Results in Materials 29 (2026) 100863

Contents lists available at ScienceDirect

Results in Materials

journal homepage: www.sciencedirect.com/journal/results-in-materials

Ab-initio investigation of optical, structural and electronic properties of the cubic perovskite $CsCdX_3$ (X= Cl, Br, I) for potential applications

Akram Aqili [a,*], Anas Y. Al-Reyahi [a], Said Al Azar [b], Saber Saad Essaoud [c,d], Mufeed Maghrabi [a], Ahmad A. Mousa [e,f], Mohammed Elamin Ketfi [g], Nabil Al-Aqtash [a], Marwan S. Mousa [h]

[a] Department of Physics, Faculty of Science, The Hashemite University, P.O. Box 330127, Zarqa, 13133, Jordan
[b] Department of Physics, Faculty of Science, Zarqa University, Zarqa, 13132, Jordan
[c] Department of Physics, Faculty of Science, University of M'sila, P.O. Box 166 Ichebilia, 28000, M'sila, Algeria
[d] Laboratory of Materials and Renewable Energy, Faculty of Science, University of M'sila, P.O.Box 166 Ichebilia, 28000, M'sila, Algeria
[e] Department of Basic Sciences, Middle East University, Amman, 11831, Jordan
[f] Applied Science Research Center, Applied Science Private University, Amman, Jordan
[g] Department of Electronics, Faculty of Technology, University of M'sila, P.O.Box 166 Ichebilia, 28000, M'sila, Algeria
[h] Department of Renewable Energy Engineering, Jadara University, Irbid, 21110, Jordan

ARTICLE INFO

Keywords:
Structural properties
$CsCdX_3$
Thermal stability
Optoelectronic properties
DFT band structure calculations

ABSTRACT

The present work falls within the framework of searching for suitable materials for use in the photovoltaic energy field to modernize solar cells more effectively. The various physical properties of the perovskite compound $CsCdX_3$ were investigated based on the effects induced by changing the type of the halogen atom Cl, Br or I. The dynamic stability of the structures was checked using phonon implemented in the VASP (Vienna Ab initio Simulation Package) code, where the computed frequencies show positive values for all vibrational modes, which means it is stable. The results demonstrate that all compounds exhibit mechanical stability. Ionic bonds predominate, and they are all isotropic and ductile. In addition, the *ab initio* calculation method was used to determine structural properties such as crystal cell constants as well as the compressibility coefficient. The electron behavior of the three compounds was identified using well-known approximations, namely GGA-PBE (Generalized Gradient Approximation - Perdew, Burke, and Ernzerhof), mBJ (modified Becke-Johnson), and YS-PBE0 (Yukawa Screened-PBE0 Hybrid Functional). The results show that the three compounds have semiconductive behavior with a tangible effect of the type of halogen atom on the energy bandgap. The investigated materials show their highest absorption in the ultraviolet region. Thermoelectric analysis indicates that the compounds have a figure of merit of about 0.75 which remains fairly stable with increasing temperature. Thus, the material can be considered in the fabrication of thermoelectric devices or as an absorber layer in the ultraviolet region.

1. Introduction

Perovskite materials have attracted considerable attention in the field of materials science due to their remarkable electrical and optical characteristics [1–6]. Perovskite minerals, named after the Russian mineralogist Lev Perovski [7], are distinguished by their ABX_3 crystal structure, with A and B are cations and X stands for an anion [8,9]. The significance of investigating perovskites originates from their broad range of applications, which include solar cells, light-emitting diodes (LEDs), sensors, and thermoelectric devices [3,6,10–15]. In addition, Perovskites exhibit tunable electrical, optical, and structural features, which position them as highly viable contenders for future technologies.

Previous investigations have established the foundation for our study by investigating several aspects of perovskite materials. Wang et al. [16] examined the thermal conductivity of cubic halide perovskites and found that they enjoy exceptionally low lattice thermal conductivity, suggesting their promise as materials with low thermal conductivity. Leger et al. [9] performed studies on the isotropic compression of

* Corresponding author.
E-mail address: akramaq@hu.edu.jo (A. Aqili).

https://doi.org/10.1016/j.rinma.2025.100863
Received 10 April 2025; Received in revised form 23 September 2025; Accepted 8 December 2025
Available online 16 December 2025

$CsCdBr_3$, a perovskite-type compound with linear chains. Their study yielded valuable information on the behavior of the bulk modulus when the material is subjected to a high-pressure environment. In addition, Ilyas et al. [17] performed a theoretical study on $CsCdCl_3$ and found interesting optical and structural parameters comparable to $CsPbCl_3$. Imran et al. [18] investigated the impact of surface passivation on maintaining the composition and emission color of $CsCd_xPb_{1-x}Br_3$ perovskite nanocrystals. Imran's study emphasizes the significance of stability and regulation in perovskite-based optoelectronic systems. Wenzel et al. [19] observed a specific absorption band of excitons that are concentrated at lattice defects, positioned underneath the lowest conduction band. The excitons, in conjunction with the low-lying conduction band, play a vital role in facilitating rapid and efficient energy transmission within the crystal. In addition, Heber et al. [20] investigated the electronic states in $CsCdBr_3$ that were both pure and doped with rare-earth elements. They noticed the existence of optically passive or "silent" states within the optical bandgap. The silent states play a crucial role in several processes, such as rapid nonradiative transitions, quantum up conversion, and increased crystal-field splitting in rare-earth dopant ions.

In the present work, the structural, dynamic stability, electrical, optical, and thermoelectric characteristics of cubic-perovskite $CsCdX_3$ were investigated, where X represents halides (Cl, Br, I). In this study, lead (Pb) was substituted with cadmium (Cd) in the $CsPbBr_3$ structure and the consequences of replacing bromine (Br) with different halides were investigated. Through an in-depth investigation of the structural, electrical, optical, and thermoelectric characteristics, our objective is to offer an important understanding of the development and enhancement of perovskite-based materials for various technological applications. This research enhances the continuous endeavors in utilizing the whole capabilities of perovskite materials for sustainable and efficient energy technologies and other applications.

The properties of perovskite materials are typically characterized through techniques including X-ray diffraction (XRD) for structural analysis, UV–Vis spectroscopy for optical band gap assessment, and spectroscopic ellipsometry for evaluating complex dielectric functions [21].

This study offers a systematic and comparative first-principles analysis of the whole halide series (X = Cl, Br, I) inside an integrated computational framework, building on key insights from previous studies on individual members of the $CsCdX_3$ family [22–24]. Our study offers novel insights that are inadequately addressed in the current literature, encompassing a thorough analysis of dynamic stability via phonon dispersion calculations, a comprehensive evaluation of mechanical properties (elastic constants, moduli, anisotropy, sound velocities, Debye temperature), an extensive investigation of optical properties across a broad energy spectrum, and the inaugural report on the thermoelectric performance of these compounds. Additionally, we utilize and evaluate many sophisticated exchange-correlation functionals (PBE, mBJ, YS-PBE0) to guarantee a reliable and precise characterization of their electrical characteristics. This thorough methodology seeks to establish a fundamental comprehension of the $CsCdX_3$ series for prospective applications in optoelectronics and renewable energy technologies [21,25–27].

2. Computational details

The Kohn-Sham equation is a powerful tool for understanding the intricate quantum-mechanical aspects of electron behavior in materials. [28]. In mathematical notation, the equation is represented as:

$$H_{KS}\ \psi_i = \epsilon_i\ \psi_i \tag{1}$$

where (H_{KS}) is the Kohn-Sham Hamiltonian, (ψ_i) represents the wavefunction of the *i-th* electron, and (ϵ_i) is the corresponding energy eigenvalue.

The solutions of the Kohn-Sham equation using different exchange-correlation approaches have been extensively studied in the literature [28–34]. Such solutions involve intricate manipulations of the Hamiltonian and the electron wavefunctions, demonstrating the quantum mechanical complexity of the electronic behavior.

The careful choice of the exchange-correlation potential is essential for the precision of predictions. In this study, we employ three distinctive functionals to examine various aspects of the material's characteristics:

The commonly utilized Perdew-Burke-Ernzerhof (PBE) functional, which employs a generalized gradient approximation (GGA), was selected for structure optimization and preliminary evaluations because to its computing efficiency, although its recognized propensity to underestimate band gaps.

The Tran-Blaha modified Becke-Johnson (TB-mBJ) potential [33] was utilized to provide enhanced accuracy in electrical band gaps and optical properties, as it efficiently rectifies the band gap underestimate inherent in regular GGA without paying the enormous computational cost associated with hybrid functionals.

The hybrid functional YS-PBE0 [35] was employed to deliver a high-level, benchmark-quality characterization of the electronic structure for all molecules, providing more rigorous analysis of exchange.

The reciprocal-lattice vectors attain a maximum value of (RMT × Kmax = 8.0). The minimum radius of Muffin Tin spheres is RMT = 2.5.

A careful selection of the exchange-correlation potential is crucial to the accuracy of predictions. The widely employed Perdew-Burke-Ernzerhof (PBE) functional [28,31,33], the PBE functional, which employs a generalized gradient approximation (GGA), was selected for structure optimization and preliminary evaluations because to its computing efficiency, although its recognized propensity to underestimate band gaps. incorporating a GGA, is characterized by the following expression:

$$E_{xc}^{PBE}[n] = \int n(r)\epsilon_{xc}^{PBE}(n(r))\ dr \tag{2}$$

where $\left(E_{xc}^{PBE}\right)$ denotes the exchange-correlation energy, $n(r)$ is the electron density, and $\left(\epsilon_{xc}^{PBE}\right)$ is the PBE exchange-correlation per particle.

The Tran-Blaha modified Becke-Johnson (TB-mBJ) potential was utilized to provide enhanced accuracy in electrical band gaps and optical properties, as it efficiently rectifies the band gap underestimate inherent in regular GGA without paying the enormous computational cost associated with hybrid functionals. In contrast, TB-mBJ potential can be expressed as:

$$V_{\text{TB-mBJ}}(r) = -\frac{1}{r}(1 - e^{-\alpha r})^2 + C_{\text{mBJ}}\frac{e^{-\beta r} - e^{-\gamma r}}{r^2} \tag{3}$$

where α, β, and γ are parameters controlling the range of the potential, and C_{mBJ} is another parameter. The utilization of these potentials in electronic structure simulations within *Wien2k* package enhances computational tools for comprehensive investigation of the material understudy.

The hybrid functional YS-PBE0 [35] was employed to deliver a high-level, benchmark-quality characterization of the electronic structure for all molecules, providing more rigorous analysis of exchange. The YS-PBE0, which is included in the *Wien2k* package, was used to precisely characterize the electronic characteristics of materials. This hybrid functional is a combination of the Perdew-Burke-Ernzerhof (PBE) exchange-correlation function with the part (α) of the exact exchange derived from the Hartree-Fock theory. The YS-PBE0 functional is formally has the following form:

$$E_{xc}^{\text{YS-PBE0}}[n] = E_x^{\text{HF}}[n] + (1-\alpha)E_x^{\text{PBE}}[n] + E_c^{\text{PBE}}[n] \tag{4}$$

where $E_x^{\text{HF}}[n]$ is the Hartree-Fock exchange energy, $E_x^{\text{PBE}}[n]$ is the exchange energy from the PBE functional, and $E_c^{\text{PBE}}[n]$ is the correlation

energy from the PBE functional. The parameter α modulates the impact of exact exchange on the overall energy, achieving a trade-off between computing efficiency and precision in electronic structure computations. The YS-PBE0 functional has been extensively used to enhance accuracy compared to typical DFT functionals.

Throughout our examination, we found that the reciprocal-lattice vectors achieve a maximum value of $(R_{MT} \times K_{max} = 8.0)$, The minimum radius of Muffin Tin spheres is $(R_{MT} = 2.5)$. Employing a $(15 \times 15 \times 15)$ An atomic force cutoff of $(1.0\ \text{mRy}/\text{Bohr})$ is used for structural optimization in a k-point mesh covering the Brillouin zone. The energy separation of the core to valence states is $(-6.0\ \text{Ry})$, where $(nn = 2)$ represents the distances to the nearest neighbors. Additionally, the charge density is expanded in the Fourier series up to is $(G_{max} = 16)$. Iterative computations persist until the convergence tolerance of energy and charge fall below (0.1 mRy) and (0.0001 e), respectively.

The Birch Murnaghan equation of state [36] has been used to find the optimal-structural properties of the considered compounds, such as lattice-constant (a), bulk-modulus (B_0), ground-state energy (E_0), and unit cell volume (V_0). Further assessments of compound stability through phonon analysis using the VASP code [37,38] depend on the optimized-structural variables that were found.

The exploration extends to compute the band structure (BS), electronic characteristics and Density of States (DOS) utilizing both PBE and mBJ exchange-correlation potentials. The bandgap calculations offer insights into the materials' electronic properties. Optical characteristics, including reflectivity $(R(\omega))$, refractive index $(n(\omega))$, and absorption coefficient $(I(\omega))$, are meticulously examined using PBE and mBJ energy exchange potentials. Both the real and imaginary parts of the complex dielectric function are calculated as well. with each equation deeply embedded in the existing literature.

The phrase "i-th" denotes the electron that is indexed as i in a series, with ψi representing its wavefunction and ϵi representing its energy eigenvalue. The parameter C_{mBJ} represents the corrected modified Becke-Johnson potential, which is utilized to enhance the accuracy of band gap predictions in Density Functional Theory (DFT) calculations. The Wien2k package is a computational software that utilizes the Full-Potential Linearized Augmented Plane Wave (FP-LAPW) approach for doing electronic structure calculations based on Density Functional Theory (DFT). Density functional theory (DFT) functionals, such as local density approximation (LDA) or generalized gradient approximation (GGA), are mathematical models used to estimate the exchange-correlation energy in DFT. The expression $R_{MT}" \times K_{max}" = 8.0$ specifies the threshold for plane-wave truncation in Wien2k. Here, RMT represents the minimum muffin-tin radius, while Kmax represents the highest reciprocal lattice vector taken into account. The parameter nn in $nn = 2$ signifies that the computations take into account interactions with the crystal structure's second nearest neighbors.

3. Results and discussion

3.1. Structural and mechanical properties

In this part, we will investigate the cubic perovskite's dynamic stability and structural properties for $CsCdX_3$ (X = Cl, Br, and I) within *Pm-3m* (#221) space-group. The unit cells corresponding to various halide compositions are shown in Fig. 1a. Geometric calculations were conducted during volume optimization to determine the optimal volume associated with the minimum energy using the PBE exchange-correlation functional. The equilibrium lattice parameter was ascertained by fitting the energy-volume curves, derived from geometric calculations during volume optimization, to the Birch-Murnaghan equation of state. The resultant curves for each combination, displaying a distinct energy minimum, are illustrated in Fig. 1b, c, and 1d. As a result of applying the Birch-Murnaghan-equation of state, the most optimal structural parameters were finally determined. (The Birch-Murnaghan equation is an empirical equation of state used to describe the relationship between pressure and volume in materials, particularly for studying compressibility under high pressure by fitting data to determine bulk modulus and its derivative [39]), and the results are tabulated in Table 1 alongside the theoretical and experimental values for comparison.

Our calculated equilibrium lattice parameters for $CsCdCl_3$ closely align with the existing data for $CsCdCl_3$ [22,40]. Our computed value (5.323 Å) exhibits a +2.2 % overestimation relative to the experimental value (5.210 Å). This is a recognized systematic inaccuracy linked to the GGA-PBE functional, which frequently marginally overestimates lattice

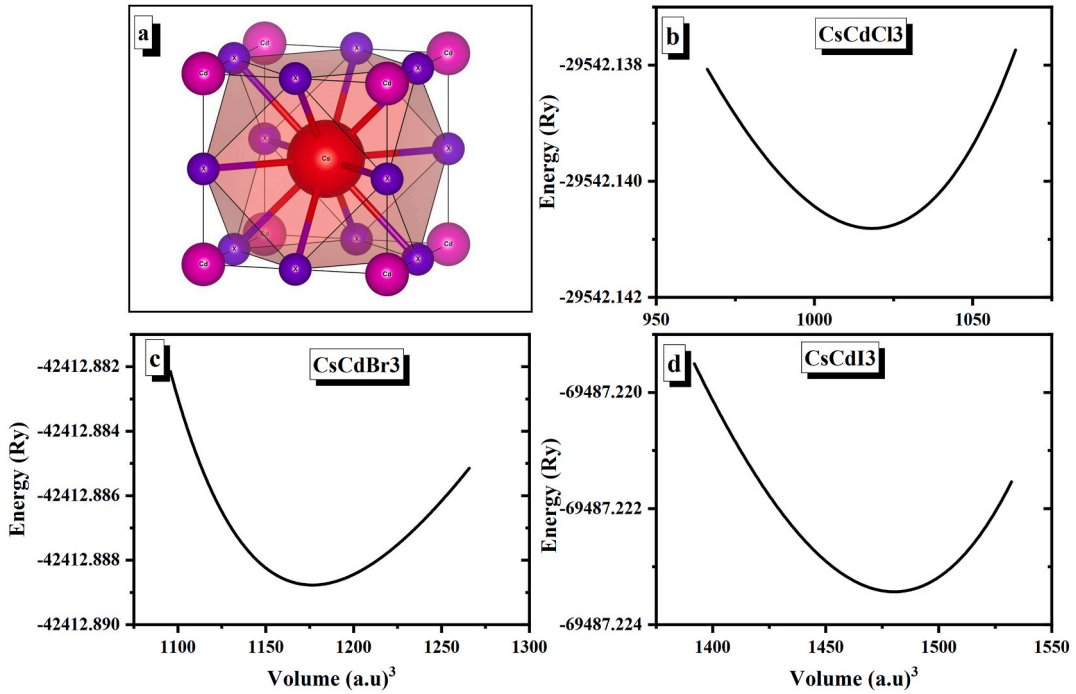

Fig. 1. a: The unit cell of $CsCd(Cl,Br,I)_3$ perovskites plotted using the VESTA software. b, c and d: the volume optimization for CsCdX3 (X = Cl, Br, and I) respectively.

Table 1
The lattice constant a (Å), optimized volume V_0 (Å^3), bulk modulus B (GPa), and the minimum energy E_0 (Ry) for *Pm-3m* (#221) of the $CsCdX_3$ (X = Cl, Br, and I) perovskites.

	Space group	a(Å)	V_0 (Å^3)	B (GPa)	E_{form} (eV/atom)	E_{coh} (eV/atom)	E_0 (Ry)
$CsCdCl_3$	Pm-3m (#221)	5.323 5.134^{LDA} [40] 5.218^{GGA} [40]5.210^{Exp} [22]	150.824	38.211, 44,49^{LDA} [40] 34.88^{GGA} [40]	−0.080	0.169	−29542.14
$CsCdBr_3$		5.587	174.396	23.926	−0.058	0.127	−42412.89
$CsCdI_3$		6.030	219.256	27.2117	−0.035	0.067	−69487.22

constants owing to its approach to electron correlation. The predicted equilibrium lattice parameter for $CsCdCl_3$ (5.323 Å) largely corresponds with previous theoretical data and matches well with the experimental result (5.210 Å), hence validating the consistency of our methods [41,42]. The systematic increase in the lattice constant when X in $CsCdX_3$ takes the sequence Cl-Br-I (from 5.323 to 6.030 Å, see Table 1) suggests that the substitution of halides impacts the unit cell dimensions. This increase is attributed to the increasing ionic size of the halide, which means an increase in the Cs-X and Cd-X bond lengths. This trend is further supported by the inverse relationship observed between the bulk modulus and the unit cell volume. Also, the bulk modulus of $CsCdBr_3$ (23.9 GPa) obtained in this study is close to the value reported by Leger et al. (21.3 GPa) [9].

The dynamic stability was investigated using the VASP code (Vienna Ab-initio Simulation Package) [43,44] to calculate phonon frequency [38,45,46]. In Fig. 2, the vibrational frequencies of the structures that were investigated and found to have the lowest energy are depicted. These frequencies exclusively exhibit positivity without any imaginary components, signifying the stability of the structures. Cohesive energy (E_{coh}) and formation energy (E_{form}) were computed to evaluate chemical and thermodynamic-stability (TS), correspondingly. The positive E_{coh} of 0.169, 0.127, and 0.067 eV/atom affirm the TS of $CsCdX_3$ (X = Cl, Br, I), whereas the negative E_{form} of −0.08, −0.058, and −0.035 eV/atom indicate the compounds' chemical stability, emphasizing their structural integrity and energetic favorability.

Understanding the compounds' mechanical properties and how they react to stresses applied to the crystal structure is the main aim of this section. An in-depth knowledge of the basic physical characteristics of the studied compounds is crucial for the engineering, and utilization of materials across various domains. The elasticity constants C_{11}, C_{12}, and C_{44} were investigated at a temperature of 0 K. The computation employed the GGA-PBE exchange-correlation potential. Three commonly acknowledged criteria, as depicted in Eq(5a, 5b and 5c), are employed to assess the elastic stability of cubic structures [47,48]. The examination of the elastic constants can provide insights into the mechanical stress characteristics of $CsCdX_3$ (X = Cl, Br, I) compounds. The Cauchy pressure (CP = C_{12} - C_{44}) is commonly used to predict atomic bonding [49,50].

$$C_{11} + 2C_{12} > 0 \tag{5a}$$

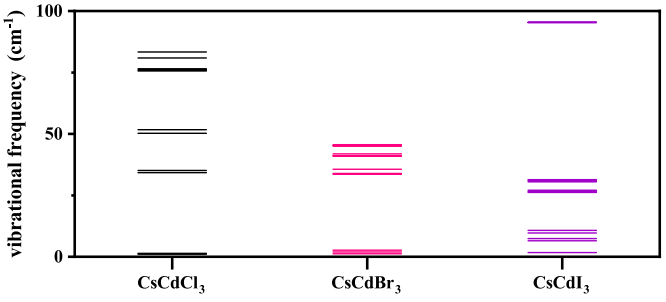

Fig. 2. The perovskites $CsCdX_3$ (X = Cl, Br, and I) phonon vibrational frequencies (3N-6) at the lowest energy as calculated using the VASP code.

$$C_{44} > 0 \tag{5b}$$

$$C_{11} - C_{12} > 0 \tag{5c}$$

Our calculated elastic constants (C_{11}, C_{12}, C_{44}) for all three compounds satisfy these conditions, confirming their mechanical stability in the cubic phase. The bulk (B), shear (G), and Young's moduli (Y) were determined for the variations anions (Cl, Br, and I) employing the median of the Voigt, Reuss, and Hill (VRH) technique [51]. In 1928, Voigt proposed a method for calculating the elastic moduli of a crystal aggregate by averaging the relations expressing stress in a single crystal in terms of the given strain (uniform strain). On the other hand, Reuss proposed averaging the relations expressing strain in terms of given stress (uniform stress). Both methods are approximate, and measured moduli for the crystal aggregate generally fall between the Voigt and Reuss values, with the former being greater. Table 2 presents the bulk modulus (B) ($B = (C_{11} - 2C_{12})/3$) values for $CsCdX_3$ (X = Cl, Br, I) in GPa. The highest values for Bulk (B), shear modulus (G), and Young's modulus (Y) are observed in $CsCdCl_3$, while the lowest values are observed in $CsCdI_3$. These values can be attributed to the size of the unit cell, with larger cells being more susceptible to pressure.

The behavior of chemical bonds depends upon the magnitude of the Poisson ratio (v). Covalent materials often exhibit a low value of v, commonly denoted as $\nu = 0.1$. The difference between G and B is minimal in these materials, with G equal to 1.1B. Ionic materials typically have a value of around 0.25 for ν and a value of 0.6B for G. In contrast, metallic-materials often have a value of $\nu = 0.33$ and G = 0.4B [52]. When the value of Poisson's ratio (ν) equals 0.5, G is equal to zero. The Poisson ratios for $CsCdX_3$ (X = Cl, Br, I) have been determined to be 0.300, 0.279, and 0.273, respectively. The values found for ν, G, and B (refer to Table 2) suggest the predominant ionic bonds in the studied

Table 2
The calculated values of the elastic constants (C_{11}, C_{12}, and C_{44}) and other mechanical properties for cubic-perovskite $CsCdX_3$.

	$CsCdCl_3$	$CsCdBr_3$	$CsCdI_3$
C_{11} (GPa)	52.366	49.850	29.920
C_{12} (GPa)	18.960	15.282	9.642
C_{44} (GPa)	11.985	11.689	7.872
Cauchy pressure $C_p = C_{12}$-C_{44} (GPa)	6.975	3.593	1.77
C_{11}-C_{12} (GPa)	33.406	34.568	20.278
C_{11}+$2C_{12}$ (GPa)	90.287	80.415	49.205
Bulk modulus *B (GPa)*	30.095	26.805	16.401
Young's modulus *Y (GPa)*	13.872	13.927	8.779
shear modulus *G (GPa)*	36.074	35.613	22.349
Poisson's ratio ν	0.300	0.279	0.273
anisotropic ratio *A*	0.7175	0.676	0.776
Pugh's index *B/G*	2.198 (Ductile)	1.960 (Ductile)	1.883 (Ductile)
longitudinal sound velocity ν_t *(m/s)*	1880.499	1720.954	1355.628
transverse sound velocity ν_l *(m/s)*	3533.823	3123.007	2431.057
average elastic sound velocity ν_m *(m/s)*	2101.137	1917.937	1509.390
Debye temperature θ_D *(K)*	200.954	174.763	127.428
Tian-Vickers hardness	2.396	2.728	2.075

compounds. Additionally, it should be noted that the Poisson ratios of the three compounds exceed 0.26, indicating their ductility. [53–55]. The anisotropic ratio (A) was also examined, with $A = 2\,C_{44}/\,(C_{11} - C_{12})$ on the right side. Crystalline substances exhibit elastic anisotropy when the value of A is greater than 1. The anisotropic ratio (A) values obtained for the examined compounds are less than 1, suggesting that the material exhibits more compressibility along one axis compared to another axis. The examined compounds were also subjected to calculations of transverse (v_s), longitudinal (v_l), and average (v_m) elastic sound velocities as given in equations (6a), (6b) and (6c).

$$v_m = \left[\frac{1}{3}\left(\frac{2}{v_s^3} + \frac{1}{v_l^3}\right)\right]^{-\frac{1}{3}} \tag{6a}$$

$$v_l = \left[\frac{B + \frac{4G}{3}}{\rho}\right]^{\frac{1}{2}} \tag{6b}$$

$$v_s = \left[\frac{G}{\rho}\right]^{\frac{1}{2}} \tag{6c}$$

where B, G, and ρ are bulk modulus, share modulus, and mass density of the material respectively. The values of the speeds that were achieved are shown in Table 2. $CsCdCl_3$ has the greatest velocity values among the three chemicals. High transverse and longitudinal velocities correlate with stiffness and deformation resistance. Similarly, the average elastic sound velocity follows the same pattern; a greater value indicates a material with more stiffness. Nevertheless, materials with higher density often exhibit higher longitudinal and transverse velocities [56]. The Pugh ratio (B/G) quantifies the degree of ductility or brittleness exhibited by a material. According to Ref. [57], ductile materials have a B/G ratio that exceeds 1.75. All compounds may be classified as ductile materials due to their B/G ratio above 1.75.

The Debye temperature (θ_D) (Eq. (7)) is a fundamental parameter that establishes the relationship between elastic characteristics and thermodynamic parameters such as vibrational entropy, specific heat, and melting temperature [58].

$$\theta_D = \frac{h}{k_B}\left[\frac{3n}{4\pi}\left(\frac{N_A\rho}{M}\right)\right]^{\frac{1}{3}} v_m \tag{7}$$

Debye temperature θ_D values for $CsCdX_3$ (X = Cl, Br, I) are 200.954 K, 174.763 K, and 127.428 K, respectively. A higher Debye temperature frequently corresponds to a higher melting point, greater thermal stability, and improved mechanical properties [59,60]. Consequently, it can be seen that $CsCdCl_3$ exhibits more robust atomic bonds and a more rigid lattice structure in comparison to the other two compounds. The mechanical strength of the compounds was determined using the Tian-Vickers hardness test (The Tian-Vickers hardness test is a theoretical approach that predicts material hardness based on first-principles calculations, correlating electronic structure and bonding characteristics with mechanical properties, serving as a computational counterpart to the traditional Vickers hardness test, which measures hardness by indenting a material with a diamond indenter [61]). The compound $CsCdX_3$ (X = Cl, Br, and I) had values of 2.396, 2.728, and 2.075, respectively. The results obtained indicate $CsCdBr_3$ is the harder chemical among those that were investigated.

3.2. Electronic properties

Fig. 3 illustrates the band structures (BS) along the high-symmetry points within the first Brillouin zone and the total density of states (TDOS) for the $CsCdX_3$ compounds, using mBJ energy exchange potentials. The bandgap values obtained from the PBE, mBJ, and YS-PBE0 are shown in Table 3. The results of the three exchange potentials demonstrate that the bandgap is reduced when X in $CsCdX_3$ takes the sequence Cl, Br, and then I due to the progressive strengthening of the covalent bond. **PBE** results severely underestimate the bandgap for all compounds. For example: i) It predicts $CsCdI_3$ to be a metal with a bandgap of **0 eV**, ii) It gives a very small gap for $CsCdBr_3$ (0.758 eV), iii) Its values for the lead-based compounds ($CsPbBr_3$, $CsPbI_3$) are also significantly lower than the experimental references. They tend to delocalize electrons too much, leading to an underestimation of the energy required to excite an electron from the valence band to the conduction band. The mBJ functional performs much better than PBE but shows a different systematic error. mBJ significantly overestimates the bandgap compared to both experimental results and the more

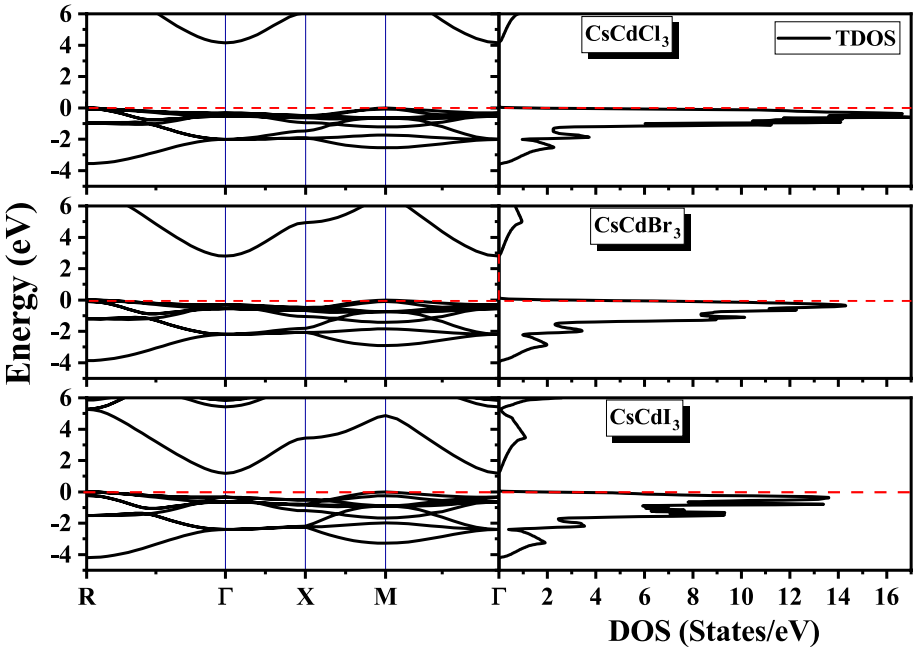

Fig. 3. The band structure (BS) and the total density of states (TDOS) for $CsCdX_3$ compounds as calculated by employing the mBJ potential.

Table 3
The perovskite $CsCdX_3$ bandgap utilizing PBE, mBJ, and YS-PBE0 exchange-correlation parameterization.

Compound	Bandgap (eV)			
	Previous study	PBE	mBJ	YS-PBE0
$CsPbBr_3$	**2.06 PBE** [66] **2.29 Exp** [67]	**1.711**	**2.923**	**2.507**
$CsPbI_3$	**1.56 PBE** [68] **1.879 mBJ** [69] **1.44 HSE06** [68] 1.70 Exp [69,70]	**1.417**	**2.124**	**2.093**
$CsCdCl_3$	1.62 LDA [40] 1.67 GGA [40] 3.77 mBJ [40]	1.740	4.200	**2.901**
$CsCdBr_3$	–	0.758	2.853	1.730
$CsCdI_3$		0	1.256	0.458

sophisticated YS-PBE0 hybrid functional. For $CsCdCl_3$: mBJ gives 4.200 eV, while the previous mBJ study cited shows 3.77 eV and YS-PBE0 gives 2.901 eV. For $CsPbBr_3$: mBJ gives 2.923 eV, which is much higher than the experimental value of ~2.29 eV and the YS-PBE0 value of 2.507 eV. While mBJ is excellent at opening the bandgap, it is not a one-size-fits-all solution. Its performance can vary depending on the material system. For these perovskites, particularly the cadmium-based ones, it appears to be overcorrecting the error inherent in PBE. The YS-PBE0 results appear to be the most accurate and reliable among the three methods used in this study. $CsCdCl_3$ has the largest bandgap (~2.9 eV with YS-PBE0). $CsCdBr_3$ has a medium bandgap (~1.73 eV with YS-PBE0). $CsCdI_3$ has the smallest bandgap (~0.458 eV with YS-PBE0). This is due to the increasing size of the halogen p-orbitals that form the valence band maximum, which leads to a higher energy level and thus a smaller gap to the conduction band. These values demonstrate the suitability of the compounds for use in solar cells as an absorption layer [62–65]. The difference between previous studies and ours might result from differences in computational parameters, such as the specific implementation of the mBJ potential, the plane-wave cutoff (RK_{max}), and the density of the k-point grid. This is a recognized systematic inaccuracy linked to the GGA-PBE functional, which frequently marginally overestimates lattice constants due to its approach to electron correlation.

The lower bands originate mainly from the X: p states, where X represents Cl, Br, and I. On the other hand, the upper bands mostly come from X: p states as well as from Cd: D_{eg} states, which are represented in the partial density of states (PDOS) shown in Fig. 4. Furthermore, there is a significant presence of hybridization coming from Cs: p, Cd: d, and X: p. Strong hybridization occurs with decreasing bandgap. The conduction band primarily originates from the state of Cd. The examined compounds' valence-band maximum (VBM) approaches the Fermi energy more than the conduction band minimum (CBM). They classify as p-type semiconductors, with holes being the main carriers. The flat VBM and curved CBM show that hole carriers at VBM have greater effective masses than electrons at CBM. The BS curves show that the studied perovskites have an indirect bandgap between (R and M to Γ) points. The band structure of $CsCdCl_3$ was computed and showed similar conduction band and valence band splitting as previously reported [40] but occurring at different energy levels. In $CsCdCl_3$, the use of PBE formed an indirect energy gap of 1.74 eV, while the mBJ and YS-BPE0 methods gave an indirect bandgap of 4.20 eV and 2.90 eV, respectively. The BPE findings agree with earlier studies that reported indirect bandgaps of 1.691 eV and 1.544 eV [71], as well as 1.62 eV and 1.67 eV [40].

3.3. Optical properties

The optical characteristics of $CsCdX_3$ (X = Cl, Br, I) have been investigated using the mBJ energy exchange potential. The parameters studied here include the complex optical conductivity (σ_{Re} and σ_{Im}) dielectric functions ($\varepsilon_1(\omega)$ and $\varepsilon_2(\omega)$), extinction coefficient k(ω), refractive index n(ω), absorption α(ω), reflectance R(ω), and energy loss function L(ω). The imaginary component of the dielectric function $\varepsilon_2(\omega)$ (Eq. (8)) was computed directly from the momentum matrix elements. The real component $\varepsilon_1(\omega)$ (Eq. (9)) was subsequently obtained from $\varepsilon_2(\omega)$ through the use of the Kramers-Kronig transformation. The imaginary component of the dielectric function, $\varepsilon_2(\omega)$ (Eq. (8)), which relates to absorption, was computed directly from the momentum matrix elements. The real component, $\varepsilon_1(\omega)$ (Eq. (9)), which describes dispersion, was subsequently obtained from $\varepsilon_2(\omega)$ via the Kramers-Kronig transformation. Other optical properties were computed using equations (8)–(15), rely on the calculated values of $\varepsilon_2(\omega)$ [72–74]. By analyzing and interpreting these parameters, we will gain insight into the optical characteristics of the compounds and their possible applications in photovoltaics, detectors, and optoelectronics [37,45,46,75–77].

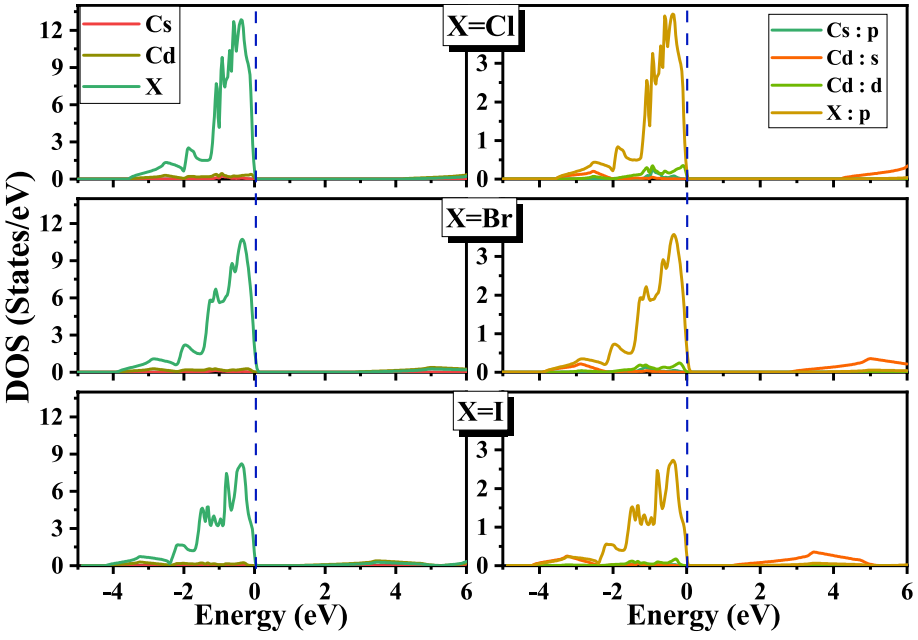

Fig. 4. The PDOS for $CsCdX_3$ compounds calculated using mBJ energy exchange approximation.

$$\varepsilon_2(\omega)=\frac{2e^2\pi}{\Omega\,\varepsilon_0}\sum_{k,V,C}\left|\langle\psi_k^C|\hat{u}\times r|\psi_k^V\rangle^2\right|\delta\left(E_k^C-E_k^V-E\right) \tag{8}$$

$$\varepsilon_1(\omega)=1+\frac{2}{\pi}P\int_0^X\frac{\omega'\,\varepsilon_2(\omega)}{\omega_2'-\omega_2}d\omega' \tag{9}$$

$$\sigma(\omega)=\frac{\omega}{4\pi}\varepsilon_2(\omega) \tag{10}$$

$$I(\omega)=\frac{\sqrt{2}\omega}{C}\left(\sqrt{\varepsilon_1^2(\omega)+\varepsilon_2^2(\omega)}-\varepsilon_1\omega\right)^{\frac{1}{2}} \tag{11}$$

$$k(\omega)=\frac{I(\omega)}{2\omega} \tag{12}$$

$$n(\omega)=\frac{1}{\sqrt{2}}\left(\varepsilon_1\omega+\sqrt{\varepsilon_1^2(\omega)+\varepsilon_2^2(\omega)}\right)^{\frac{1}{2}} \tag{13}$$

$$R(\omega)=\frac{n(\omega)+iK(\omega)-1}{n(\omega)+iK(\omega)+1} \tag{14}$$

$$L(\omega)=Im\left(\frac{\varepsilon_2(\omega)}{\varepsilon_1^2(\omega)+\varepsilon_2^2(\omega)}\right)=Im\left(-\frac{1}{\varepsilon(\omega)}\right) \tag{15}$$

Fig. 5 shows that the static real dielectric function $\varepsilon_1(0)$ for $CsCdCl_3$, $CsCdBr_3$, and $CsCdI_3$ have the values of 2.19, 2.55, and 3.57, respectively. The dielectric constant of $CsCdBr_3$ is lower than that of $CsPbBr_3$ [78]. Similar compounds have shown the inversely relationship between $\varepsilon_1(0)$ and the obtained bandgap. In the visible range, the dielectric constants remain remarkably constant. The point at which they become negative indicates a transition to metallic behavior. The patterns of the imaginary part of the dielectric functions $\varepsilon_2(\omega)$ of these compounds are quite similar, with only little variations in the locations and sizes of the peaks. At lower energy, $CsCdI_3$ shows the most intense peak. Its value increases with increasing photon energy, peaking at 12.77, 8.89, and 6.85 eV for chlorine, bromine, and iodide compounds, respectively. The optical bandgap values for $CsCdCl_3$, $CsCdBr_3$, and $CsCdI_3$ are 4.41, 2.97, and 1.26 eV, respectively, As derived from the imaginary dielectric function $\varepsilon_2(\omega)$ threshold.

At photon energies of 12.77, 11.35, and 8.89 eV for chlorine, bromine, and iodide compounds, respectively, the imaginary optical conductivity becomes zero, mirroring the structure of the real part of the dielectric function. The real part of optical conductivity follows the same trend as the dielectric function.

Fig. 6 displays the refractive index, extinction coefficient, reflectivity, absorption coefficient, and energy loss as a function of photon energy. For $CsCdCl_3$, $CsCdBr_3$, and $CsZnCdI_3$, the corresponding static (low photon frequency) refractive indexes are 1.44, 1.63, and 1.91, respectively. The extinction begins at the optical bandgap as mentioned before and follows the same pattern as $\varepsilon_1(\omega)$. The reflectivity graphs indicate that all three compounds have very low photon frequency reflectivity, 5.5 % for $CsCdCl_3$, 11 % for $CsCdBr_3$, and 18 % for $CsCdI_3$. Usually, reflectivity increases as metallic behavior increases, reaching its maximum value at the lowest negative value of the real part of the dielectric constant [17]. In this case, the compound with the lowest bandgap has the maximum reflectivity. The absorption coefficient is directly related to the electronic and optical properties of the material and its applications. According to the absorption coefficient graphs, the compounds have very little absorption in the infrared (IR) and visible regions (VR) of the light spectrum, which demonstrates their

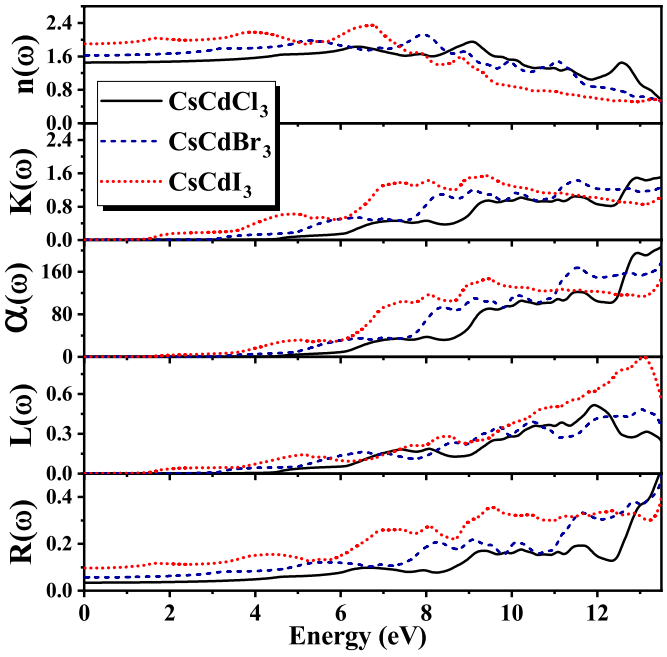

Fig. 6. The refractive index, extinction coefficient, absorption coefficient, energy loss factor and reflectivity for $CsCdX_3$ using mBJ energy exchange approximation.

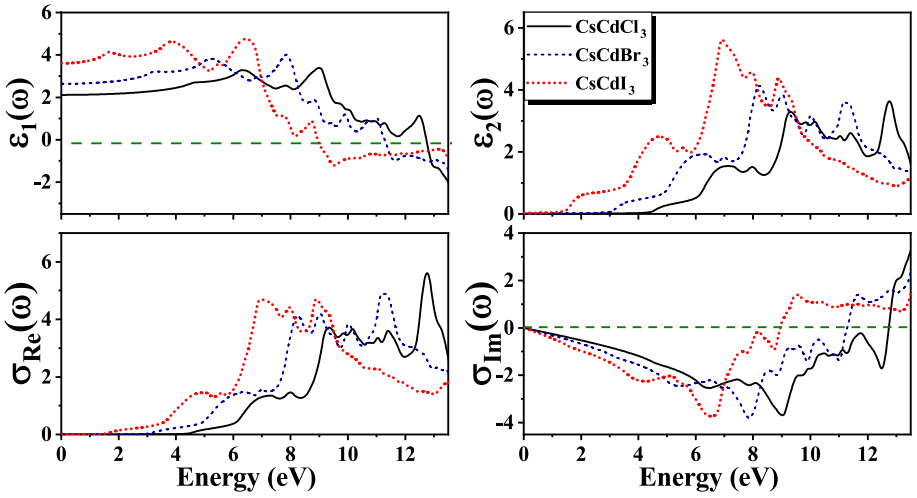

Fig. 5. The Real and the imaginary parts of the dielectric function (upper graphs) and the real and the imaginary parts of optical conductivity (lower graphs) for $CsCdX_3$ applying mBJ energy exchange approximation.

transparency characteristics in this region. The energy loss, which depends on the band structure and crystal momentum, increases as the photon energy increases. This happens often whenever photons achieve energies greater than the bandgap.

The static refractive index n(0) values for $CsCdX_3$ correspond with the band gap, with $CsCdI_3$ exhibiting the largest n(0) (~1.91) and $CsCdCl_3$ the lowest (~1.44). The values are analogous to those documented for other halide perovskites; for example, the n(0) for $CsCdBr_3$ is lower to that of $CsPbBr_3$, matching with its greater estimated band gap. The low reflectivity in the infrared and visible spectra (<18 %) and negligible absorption underscore the potential transparency of these compounds, rendering $CsCdBr_3$ and $CsCdCl_3$ appropriate for use as window layers in solar cell devices. The absorption onset, ascertained from the Tauc plot (Fig. 7D-F), validates the direct band gap characteristics of these materials.

At the absorption edge, the E_g for the allowed direct transition can be determined using $\alpha h\nu \sim (h\nu - E_g)^{1/2}$ [79], where α represents the absorption coefficient, h is the Planck constant, and ν is the frequency of the photon. The energy gap is determined by graphing the square of (αhν) vs the energy of the incident photon (E = hν) and identifying the point where a straight line intersects the x-axis, as seen in Fig. 7. The optical band gap spans 1.67 eV for $CsCdI_3$ to 4.5 eV for $CsCdCl_3$. These compounds are direct band semiconductors and have potential applications in solar cells. $CsCdI_3$ can be used as an absorption layer, while $CsCdBr_3$ can be used as a window layer for heterojunction solar cells.

The real component of the refractive index, below the point where absorption occurs, can be accurately represented by a single oscillator equation, referred to as Eq. (16). This equation has been observed to provide the most accurate match for the refractive index of most semiconducting materials [79,80].

$$n^2 = 1 + \frac{E_m E_d}{E_m^2 - (h\nu)^2} \tag{16}$$

where E_m and E_d are oscillators and dispersive energies, respectively. Fig. 7 fits the single oscillator model well, as do other conventional semiconductors.

4. Conclusions

The density functional theory was adopted to study the physical properties of $CsCdX_3$ compounds (X = Cl, Br, I) in their cubic structural phase, and to evaluate their thermoelectric performance based on the semi-classical theory of Boltzmann. The results of this study confirmed that the investigated compounds are thermodynamically stable based on the negative enthalpies values. In addition, the positive frequencies of the vibrational patterns at Γ point indicate that the studied perovskites are dynamically stable. The results demonstrate that all compounds exhibit mechanical stability. Ionic bonds predominate, and they are all isotropic and ductile. Electronically, it was shown, through the use of appropriate approximations (YS-PBE0 and mBJ), that the energy bandgap fluctuations are limited between 0.45 and 2.9 eV. Regarding the optical properties of the compounds involved in the study, the compounds had little absorption in the infrared and visible regions of the light spectrum. The thermoelectric parameters show minimal differences between the compounds based on the type of the halogen atom. The figure of merit of the studied compounds fluctuates between 0.75 and 0.8 for the entire temperature range. The heterojunction solar cells consist of an absorption layer with a bandgap matching the requirement to absorb the maximum amount of the sun spectrum. Another layer called the window layer, with different conductivity types, is located on the absorption layer which could be from other material with a wide bandgap used to allow the photon to pass to the absorption layer. In our case, $CsCdI_3$ could utilized as an absorption layer and $CsCdBr_3$ and $CsCdCl_3$ could be used as a window layer.

CRediT authorship contribution statement

Akram Aqili: Writing – review & editing, Writing – original draft, Supervision, Software, Methodology, Investigation, Formal analysis. **Anas Y. Al-Reyahi:** Writing – review & editing, Software, Formal analysis. **Said Al Azar:** Software, Methodology. **Saber Saad Essaoud:** Writing – review & editing, Formal analysis, Data curation. **Mufeed Maghrabi:** Writing – review & editing, Conceptualization. **Ahmad A. Mousa:** Writing – review & editing, Methodology. **Mohammed Elamin**

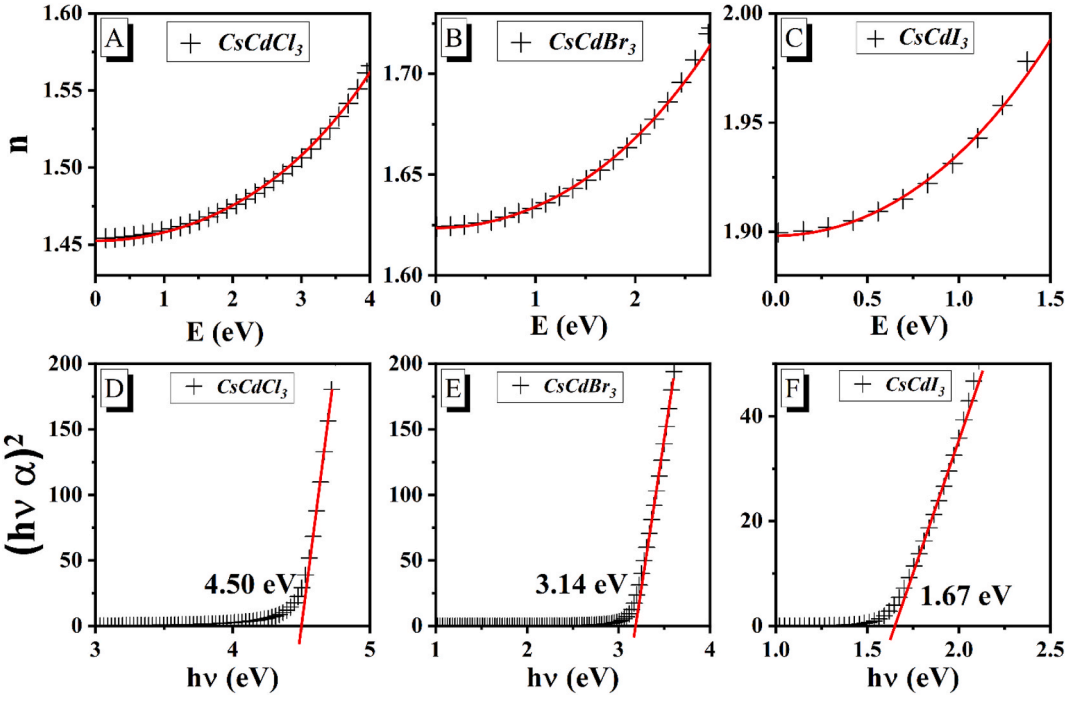

Fig. 7. The refractive index of $CsCdI_3$, $CsCdBr_3$, and $CsCdCl_3$ fits the single oscillator model (A, B, and C) and *Tauc plot of* $(\alpha h\nu)^2$ versus $h\nu$ for $CsCdI_3$, $CsCdBr_3$, and $CsCdCl_3$ (D, E, and F).

Ketfi: Software, Investigation. **Nabil Al-Aqtash:** Writing – review & editing, Software, Formal analysis, Conceptualization. **Marwan S. Mousa:** Writing – review & editing.

Declaration of competing interest

The authors declare that they have no known competing financial interests or personal relationships that could have appeared to influence the work reported in this paper.

Acknowledgment

The financial support provided by Hashemite University and Zarqa University are gratefully acknowledged.

Data availability

Data will be made available on request.

References

[1] X.-G. Zhao, G.M. Dalpian, Z. Wang, A. Zunger, Phys. Rev. B 101 (2020) 155137.
[2] G. Moschou, A. Koliogiorgos, I. Galanakis, Phys. Status Solidi 215 (2018).
[3] M. Zhang, G. Xiang, Y. Wu, J. Liu, J. Leng, C. Cheng, H. Ma, Opt. Express 31 (2023) 28624.
[4] T. Oku, Rev. Adv. Mater. Sci. 59 (2020) 264–305.
[5] B. Yu, S. Tan, D. Li, Q. Meng, Mater. Future 2 (2023) 032101.
[6] S.M.H. Qaid, B.A. Al-Asbahi, H.M. Ghaithan, M.S. AlSalhi, A.S. Al dwayyan, J. Colloid Interface Sci. 563 (2020) 426–434.
[7] W.-J. Xu, S. Kopyl, A. Kholkin, J. Rocha, Coord. Chem. Rev. 387 (2019) 398–414.
[8] A.Y. Al-Reyahi, S.M. Al Azar, S. Saad Essaoud, M. Elamin Ketfi, M. Maghrabi, Results Phys. 65 (2024) 107980.
[9] J.M. Leger, A.M. Redon, C. Andraud, F. Pelle, Phys. Rev. B 41 (1990) 9276–9282.
[10] L. Bellaiche, D. Vanderbilt, Phys. Rev. B 61 (2000) 7877–7882.
[11] J.W. Simatupang, F.M. Simanjuntak, D.J. Tyler, Perovskite Ceramics, Elsevier, 2023, pp. 485–516.
[12] M. Ahmad, G. Rehman, L. Ali, M. Shafiq, R. Iqbal, R. Ahmad, T. Khan, S. Jalali-Asadabadi, M. Maqbool, I. Ahmad, J. Alloys Compd. 705 (2017) 828–839.
[13] K. Radja, B.L. Farah, A. Ibrahim, D. Lamia, I. Fatima, B. Nabil, A. Mohamed, Y. Al-Douri, A.F.A. El-Rehim, J. Phys. Chem. Solid. 167 (2022) 110795.
[14] B. Wang, A. Navrotsky, Thermochim. Acta 695 (2021) 178813.
[15] Q.A. Akkerman, S.G. Motti, A.R. Srimath Kandada, E. Mosconi, V. D'Innocenzo, G. Bertoni, S. Marras, B.A. Kamino, L. Miranda, F. De Angelis, A. Petrozza, M. Prato, L. Manna, J. Am. Chem. Soc. 138 (2016) 1010–1016.
[16] X. Wang, Y. Zhao, S. Zeng, Z. Wang, Y. Chen, J. Ni, Phys. Rev. B 105 (2022) 014310.
[17] B.M. Ilyas, B.H. Elias, Phys. B Condens. Matter 510 (2017) 60–73.
[18] M. Imran, J. Ramade, F. Di Stasio, M. De Franco, J. Buha, S. Van Aert, L. Goldoni, S. Lauciello, M. Prato, I. Infante, S. Bals, L. Manna, Chem. Mater. 32 (2020) 10641–10652.
[19] M. Wenzel, M. Altwein, R. Demirbilek, B. Leu, J. Heber, J. Kübler, B. Bleeker, A. Meijerink, J. Alloys Compd. 300–301 (2000) 479–482.
[20] J. Heber, R. Demirbilek, M. Altwein, J. Kübler, B. Bleeker, A. Meijerink, Radiat. Eff. Defect Solid 154 (2001) 223–229.
[21] M. Pradeep, A. Cecil, N. Suresh, R. Govindasamy, N. Thirumalaivasan, J. Oral Biol. Craniofac. Res. 15 (2025) 1408–1414.
[22] R.L. Moreira, A. Dias, J. Phys. Chem. Solid. 68 (2007) 1617–1622.
[23] C. Moure, O. Peña, Prog. Solid State Chem. 43 (2015) 123–148.
[24] A.Y. Al-Reyahi, A. Mufleh, S.M. Al Azar, M. Maghrabi, N. Al Aqtash, S.S. Essaoud, K. Berarma, A. Shaheen, M.E. Ketfi, A.A. Mousa, Solid State Sci. 148 (2024) 107435.
[25] H. Saadi, H. Kerrai, L. Nait Aouzal, A. Zaim, M. Kerouad, M. El Bouziani, Phys. Lett. 531 (2025) 130175.
[26] H. Kerrai, A.A. M'hid, E.M. Jalal, H. Saadi, R. El Mrabet, A. Zaim, M. Kerouad, Mater. Today Chem. 48 (2025) 102881.
[27] H. Saadi, H. Kerrai, E.M. Jalal, M. El Bouziani, Vacuum 236 (2025) 114149.
[28] P. Blaha, K. Schwarz, F. Tran, R. Laskowski, G.K.H. Madsen, L.D. Marks, J. Chem. Phys. 152 (2020) 074101.
[29] A.D. Becke, E.R. Johnson, J. Chem. Phys. 124 (2006).
[30] F. Tran, P. Blaha, M. Betzinger, S. Blügel, Phys. Rev. B Condens. Matter 91 (2015).
[31] F. Tran, P. Blaha, Phys. Rev. Lett. 102 (2009) 226401.
[32] J.P. Perdew, in: AIP Conf Proc, AIP, 2001, pp. 1–20.
[33] D.J. Singh, Phys. Rev. B 82 (2010) 205102.
[34] D. Koller, P. Blaha, F. Tran, J. Phys. Condens. Matter 25 (2013) 435503.
[35] F. Tran, D. Koller, P. Blaha, Phys. Rev. B 86 (2012) 134406.
[36] B.F. D Murnaghan, The Compressibility of Media Under Extreme Pressures, Univ. Texas Public, 1915.
[37] Y.M. Odeh, S.M. Azar, A.Y. Al-Reyahi, A.A. Mousa, E.K. Jaradat, N. Al Aqtash, AIP Adv. (2023) 13.
[38] A. Togo, I. Tanaka, Scr. Mater. 108 (2015) 1–5.
[39] R. Jeanloz, Phys. Rev. B 38 (1988) 805–807.
[40] G. Murtaza Hayatullah, R. Khenata, S. Mohammad, S. Naeem, M.N. Khalid, A. Manzar, Phys. B Condens. Matter 420 (2013) 15–23.
[41] J.P. Perdew, K. Burke, M. Ernzerhof, Phys. Rev. Lett. 77 (1996) 3865–3868.
[42] J. Hafner, J. Comput. Chem. 29 (2008) 2044–2078.
[43] J. Hafner, G. Kresse, Properties of Complex Inorganic Solids, Springer US, Boston, MA, 1997, pp. 69–82.
[44] G. Kresse, J. Hafner, Phys. Rev. B 49 (1994) 14251–14269.
[45] A.Y. Al-Reyahi, S. Al Azar, A.A. Mousa, S.S. Essaoud, M. Maghrabi, K. Berarma, A. Aqili, A. Mufleh, H.I. Abu Radwan, Comput. Condens. Matter 34 (2023) e00787.
[46] M. Maghrabi, A.Y. Al-Reyahi, N. Al Aqtash, S.M. Al Azar, A. Shaheen, A. Mufleh, B. Shaban, Mater. Today Commun. 37 (2023) 107541.
[47] J. Wang, S. Yip, S.R. Phillpot, D. Wolf, Phys. Rev. Lett. 71 (1993) 4182–4185.
[48] A. Aqili, A.Y. Al-Reyahi, S.M. Al Azar, S. Saad Essaoud, M. Elamin Ketfi, M. Maghrabi, N. Al Aqtash, A. Mufleh, Comput. Theor. Chem. 1238 (2024) 114721.
[49] D.G. Pettifor, Mater. Sci. Technol. 8 (1992) 345–349.
[50] D. Nguyen-Maxh, D.G. Pettifor, S. Znam, V. Vitek, MRS Proc. vol. 491 (1997) 353.
[51] R. Hill, Proc. Phys. Soc. Sect. A vol. 65 (1952) 349–354.
[52] J. Haines, J. Léger, G. Bocquillon, Annu. Rev. Mater. Res. 31 (2001) 1–23.
[53] M.A. Hadi, J. Phys. Chem. Solid. 138 (2020) 109275.
[54] N. Arikan, G. DikiCi Yildiz, Y.G. Yildiz, A. İyigör, J. Electron. Mater. 49 (2020) 3052–3062.
[55] J. Wang, Y. Zhou, Phys. Rev. B 69 (2004) 214111.
[56] W. Callister Jr., D. Rethwisch, Materials Science and Engineering: An Introduction, tenth ed., WILEY, 2018.
[57] S.F. Pugh, London, Edinburgh Dublin Phil. Mag. J. Sci. 45 (1954) 823–843.
[58] S. Al-Qaisi, D.P. Rai, T. Alshahrani, R. Ahmed, B.U. Haq, S.A. Tahir, M. Khuili, Q. Mahmood, Mater. Sci. Semicond. Process. (2021) 128.
[59] Z. Guo, X. Yang, Mater. Res. Express 6 (2019) 115034.
[60] J. Spreadborough, J.W. Christian, Proc. Phys. Soc. 74 (1959) 609–615.
[61] Y. Tian, B. Xu, Z. Zhao, Int. J. Refract. Metals Hard Mater. 33 (2012) 93–106.
[62] B.R. Sutherland, Joule 4 (2020) 984–985.
[63] S. Hu, C. Xiang, S. Haussener, A.D. Berger, N.S. Lewis, Energy Environ. Sci. 6 (2013) 2984.
[64] L. Huo, X. Guo, S. Zhang, Y. Li, J. Hou, Macromolecules 44 (2011) 4035–4037.
[65] M.E. Ketfi, S.S. Essaoud, S. Al Azar, A.Y. Al-Reyahi, J. Inorg. Organomet. Polym. Mater. 34 (2024) 4622–4631.
[66] D.B. Straus, R.J. Cava, ACS Appl. Mater. Interfaces 14 (2022) 34884–34890.
[67] M. Aktary, M. Kamruzzaman, R. Afrose, RSC Adv. 12 (2022) 23704–23717.
[68] M. Afsari, A. Boochani, M. Hantezadeh, Optik (Stuttg) 127 (2016) 11433–11443.
[69] L.-K. Gao, Y.-L. Tang, ACS Omega 6 (2021) 11545–11555.
[70] G.E. Eperon, S.D. Stranks, C. Menelaou, M.B. Johnston, L.M. Herz, H.J. Snaith, Energy Environ. Sci. 7 (2014) 982.
[71] B. Ghebouli, M.A. Ghebouli, M. Fatmi, A. Bouhemadou, Solid State Commun. 150 (2010) 1896–1901.
[72] B. Li, Y. Duan, M. Peng, Vacuum 208 (2023) 111745.
[73] B. Li, H. Qi, Y. Duan, M. Peng, Mater. Sci. Semicond. Process. 160 (2023) 107400.
[74] C. Yang, Y. Wu, Y. Duan, Mater. Today Commun. 30 (2022) 103115.
[75] A.Y. Al-Reyahi, A. Mufleh, S.M. Al Azar, M. Maghrabi, N. Al Aqtash, S.S. Essaoud, K. Berarma, A. Shaheen, M.E. Ketfi, A.A. Mousa, Solid State Sci. (2023) 107435.
[76] K. Berarma, S. Sâad Essaoud, S. Al Azar, A.Y. Al-Reyahi, A.A. Mousa, A. Mufleh, Phase Transitions 96 (2023) 806–821.
[77] N. Al Aqtash, S.M. Al Azar, A.Y. Al-Reyahi, A. Mufleh, M. Maghrabi, S.S. Essaoud, K. Berarma, A.A. Mousa, Mol. Simul. (2023) 1–12.
[78] R. Rajeswarapalanichamy, A. Amudhavalli, R. Padmavathy, K. Iyakutti, Mater. Sci. Eng., B 258 (2020) 114560.
[79] A.K.S. Aqili, Z. Ali, A. Maqsood, J. Cryst. Growth 317 (2011) 47–51.
[80] A.K.S. Aqili, Z. Ali, A. Maqsood, Appl. Surf. Sci. 167 (2000) 1–11.